ELEKTRİK, VOL.6, NO.3, 1998, ©TÜBİTAK

Imaging electrical current density using nuclear magnetic resonance

B. Murat Eyüboğlu*, Ravinder Reddy and John S. Leigh
Department of Radiology, University of Pennsylvania,
Philadelphia, PA 19104, U.S.A.

Abstract

In this study, images of nonuniform and uniform electric current density in conductor phantoms, which contain magnetic resonance active nuclei, are produced using Magnetic Resonance Imaging (MRI). A standard spin echo pulse sequence is used, with the addition of a bipolar current pulse. The flux density parallel to the main magnetic field, generated by the current pulse, is encoded in the phase of the complex MR image. The spatial distribution of magnetic flux density is extracted from the phase image. Current density is calculated using the magnetic flux density. This fairly recent technique is known as Magnetic Resonance Current Density Imaging (MRCDI).

In this paper, images of magnetic flux density, generated by uniform and nonuniform current flow, and the current density image of a uniform current flow are given. Current density levels as low as $1\mu A/mm^2$ *are measured. Effects of current density on k-space data are also discussed.*

1. Introduction

Imaging of electric current density may have potential biomedical applications. For example, behavior of externally applied electric fields to the body, such as defibrillation current fields [1, 3] can be better understood, lead-sensitivity [4] maps for biopotential recordings (such as EEG, and ECG) and impedance measurements can be determined. Accurate determination of current density may also lead to accurate conductivity images [5].

In this study, electrical current density distributions - created by an externally applied dc current pulse to volume conductor phantoms - are imaged using Magnetic Resonance Imaging (MRI). The possibility of using MRI to image current density inside a volume conductor, which contains Nuclear Magnetic Resonance (NMR) active nuclei, has been demonstrated by Joy et al. [6] and Scott et al. [7, 8]. The lowest current density measured in these studies has been reported as $2.4\mu A/mm^2$. In this work, current densities as low as $1\mu A/mm^2$ are imaged. Images given in the literature [6,7,8] are of cross sections away from the current injecting electrodes. In this study, current density near the electrodes is also imaged. It is important to quantify the current density just underneath the electrodes since high current densities in the vicinity of the electrodes may result in tissue damage. Moreover, measurement of current density distribution near the current injecting electrodes provides information on the behavior of the electrode-tissue interface.

* Correspondence address: Department of Electrical and Electronics Engineering, Middle East Technical University, 06531 Ankara-TURKEY.

The theory of the effect of electric current flow on the spin echo signal and the relation between the electric current and the phase image are given in Section 2. In Section 3, imaging hardware, experimental phantoms, and the imaging pulse sequence are described. In Section 4, calculation of magnetic flux density from phase images and calculation of current density from flux density images are explained. Results of the experimental studies for uniform and nonuniform current flow are presented in Section 5. The effect of increased current density on k-space data is examined and the cause of variations in k-space are discussed in Section 5. Finally, the conclusions can be found in Section 6.

2. Theory

When noise-free NMR data without spin relaxation is assumed and the geometric distortions are neglected, the acquired NMR signal in a spin echo imaging experiment can be expressed as follows [9],

$$S\left(k_x, k_y, t\right) = \int_x \int_y M(x,y) exp\left\{j\left[\gamma B t + \phi_c + k_x x + k_y y\right]\right\} dxdy. \tag{1}$$

In this equation, $M(x,y)$ is the continuous real transverse magnetization, B is the inhomogeneity component of the magnetic field and ϕ_c is a constant phase due to instrumentation and receiver circuits. $k_x = \gamma G_x t$ and $k_y = \gamma G_y t_y$, where G_x and G_y are frequency encoding and phase encoding gradient strengths, respectively. γ is the gyromagnetic ratio, t_y is the duration of the G_y gradient pulse and t is the data acquisition time. The integrations are performed over the data acquisition window. Magnetization density can be reconstructed by Fourier transforming $S(k_x, k_y)$ with respect to k_x and k_y,

$$M_c(x,y) = \int_{kx} \int_{ky} S\left(k_x, k_y, t\right) exp\left[-j(k_x x + k_y y)\right] dk_x dk_y. \tag{2}$$

This results in a complex MR image,

$$M_c(x,y) = M(x,y) exp[j\gamma B t + j\phi_c]. \tag{3}$$

When static electric current is applied to a conductor, a constant magnetic field is generated. If the conductor contains NMR active nuclei and the application of electric current is synchronized with the MRI pulse sequence, then the component of the magnetic flux density (generated by the current flow) parallel to the main imaging field, B_0, accumulates a phase in the spin echo signal [7, 10, 11]. The acquired signal of Equation (1) becomes:

$$S\left(k_x, k_y, t\right) = \int_x \int_y M(x,y) exp\left\{j\left[\gamma B t + \phi_c + \gamma B_j\left(x,y\right) T_c + (k_x x + k_y y)\right]\right\} dxdy \tag{4}$$

where B_j is the component of the magnetic flux density parallel with B_0. T_c is the duration of the externally applied current. Current is applied in the form of a bipolar current pulse. The imaging pulse sequence and the bipolar current pulse are discussed in detail, in Section 3.3. Fourier transforming Equation (4) with respect to k_x and k_y, the complex Magnetic Resonance (MR) image is determined as,

$$M_{cj}(x,y) = M_j(x,y) exp\{j\gamma[Bt + B_j(x,y)T_c] + j\phi_c\}. \tag{5}$$

Inhomogeneities in the phase may be introduced by the imperfections in the main imaging field, the gradient fields, and/or the pulse sequence. Dividing the the complex image with the current flow, by the complex image without the current flow, effects of the phase inhomogeneities and other image artefacts are eliminated,

$$\frac{M_{cj}(x,y)}{M_c(x,y)} = \frac{M_j(x,y)exp\{j\gamma[Bt+B_j(x,y)T_c]+j\phi_c\}}{M(x,y)exp[j\gamma Bt+j\phi_c]} = exp[j\gamma B_j(x,y)T_c]. \quad (6)$$

In Equation (6), M_j and M are equal; therefore, the phase of the ratio in Equation (6),

$$\phi_{jn}(x,y) = \gamma B_j(x,y)T_c \quad (7)$$

is equal to the phase that is introduced by the current flow. ϕ_{jn} will be referred to as the normalized phase image from now on. The units for B_j and T_c are in Tesla and seconds, respectively. Since proton imaging is utilized, the gyromagnetic ratio is equal to $26753 \cdot 10^4 radiansec^{-1}Tesla^{-1}$. B_j can be determined from the normalized phase image based on Equation (7).

Assuming static current flow (i.e., the displacement current and magnetic induction are negligible), electric current density, $\vec{J}$, is related to the magnetic flux density, $\vec{B}$, by Ampere's law,

$$\vec{J} = \frac{(\nabla \times \vec{B})}{\mu_0}. \quad (8)$$

Where $\nabla\times$ represents the curl operation and μ is replaced with $\mu_0 = 4\pi 10^{-7} Hm^{-1}$ (the permeability of free space), since materials with low magnetic susceptibility are used. In order to calculate the current density component in one direction using Equation (8), magnetic flux densities in two orthogonal directions in the plane perpendicular to the direction of the current density are required. To determine components of the current density in all three orthogonal directions, magnetic flux density in all three directions must be measured. Therefore, the imaging sequence must be repeated three times. Each time, one of the three orthogonal axis of the object must be aligned with the direction of B_o. By doing so, three orthogonal components of B_j can be determined.

3. Experimental Set-up

3.1. Hardware

This study is performed on an Oxford 2.0 Tesla - 1 meter bore magnet, interfaced to a custom built MR spectrometer. A 135mm diameter cosine coil [12, 13] is used as an RF-coil which is tuned to 86.1MHz. The cosine coil provides a homogeneous excitation across the sample.

3.2. Phantoms

Two cylindrical test phantoms with different internal geometries are used in the experiments. The phantoms are shown schematically in Figure 1. Both phantoms are filled with 9g/l NaCl, 1g/l $CuSO_4 \cdot 5H_2O$ solution in water. Two 19mm diameter, 1mm thick copper disc electrodes are placed at both ends of the cylindrical phantoms. The current pulses are delivered by shielded cables which are connected to the electrodes via silver plated BNC connectors. During the data acquisition, all the wires are held at a fixed positions. Phantoms are kept at a fixed position inside the cosine coil by means of a styro foam mold.

The homogeneous conductivity phantom is a cylinder with a diameter of 77mm and a height of 70mm (Figure 1 (a)). Current spreads out from one electrode into the entire volume and converges to the electrode at the other end of the phantom, resulting in a nonuniform current density distribution.

The second test phantom is made of two concentric cylinders with a height of 65mm (Figure 1(b)). Diameters of the inner and the outer cylinders are 21mm and 69mm, respectively. Electrodes cover almost

the entire cross section at the ends of the inner cylinder; therefore, current is forced to flow uniformly in the inner cylinder. Both cylinders are filled with the same solution, but they are electrically isolated.

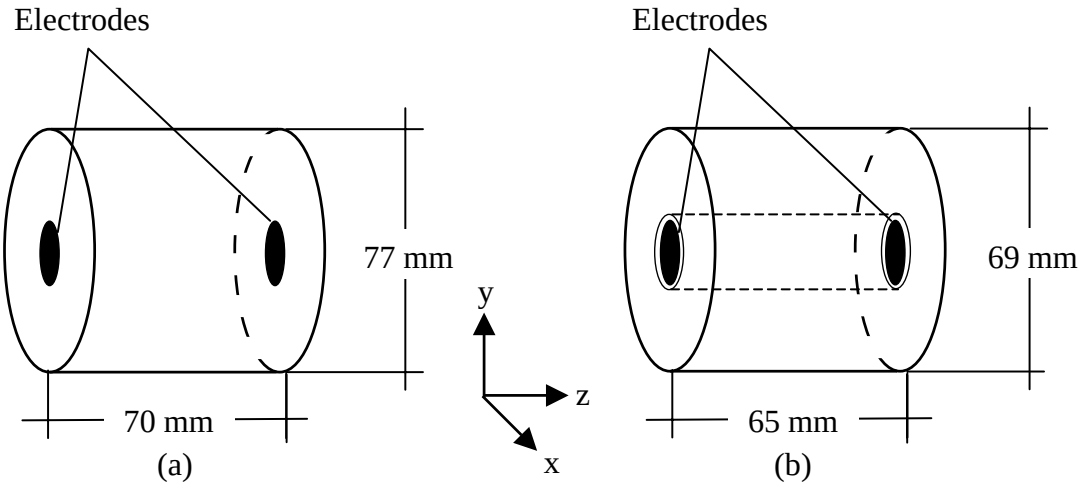

Figure 1. Geometry of the test phantoms, (a) Uniform conductivity test phantom, (b) non-uniform conductivity test phantom.

3.3. Pulse Sequence

The imaging sequence is a standard spin echo pulse sequence with an addition of a bipolar current pulse, following the slice selective 90^o pulse (Figure 2). The slice selective pulse is a 3 millisecond long truncated sinc pulse. Application of the current pulse, following the 90^o pulse, imparts additional phase to the spins. When the spins are flipped by a 180° pulse, the phase introduced by the current flow will be dephased if the polarity of the current remains the same. Therefore, the polarity of the current pulse is reversed in synchrony with application of the 180° pulse. The echo signal is sampled at 256 points for 128 phase encodings. The frequency encoding is approximately 132Hz/mm. The slice thickness is approximately 9mm. The field of view is approximately 218mm. The pulse repetition time (TR) is 1 second, the echo time (TE) is 105 milliseconds and the duration of the current pulse is 63.5 milliseconds.

4. Processing of the MR Data

Two sets of complex MR images are acquired, one with no current pulse and the other with the current pulse. The phase introduced by the current flow is extracted by taking the ratio of the second image to the first image, as in Equation (6). Normalized phase image is then related to B_j by Equation (7), after phase unwrapping.

4.1. Processing of the Phase Images

Examples of magnitude and normalized phase images are shown in Figure 3 (a), (c) and (b), (d) respectively. Images of Figure 3 (a) and (b) are transverse plane images which are acquired from the test phantom of Figure 1 (b). Images of Figure 3 (c) and (d) are longitudinal plane images which are acquired from the

test phantom of Figure 1 (a). Electrodes are visible at both ends of the phantom in Figure 3 (c). Current spreads out into the entire volume from one electrode and converges towards the electrode at the other end of the phantom.

As in Figure 3 (b) and (d), the phase of a complex MR image may range between $-\pi$ and π. These 2π phase wraps must be removed before calculating the magnetic flux density. Phase unwrapping is performed by utilizing a model-based phase unwrapping method which represents the unwrapped phase function by a truncated Taylor Series and a residual function, as described by Liang [14]. The spatial phase term can then be related to the magnetic flux density B_j based on Equation (7). Figure 4 (a) and (b) are the images of $B_x(x, y)$ (magnetic flux density in the x-direction that is generated by the externally applied electric current), and $B_y(x, y)$ (magnetic flux density in the y-direction that is generated by the externally applied electric current) measured from the concentric phantom.

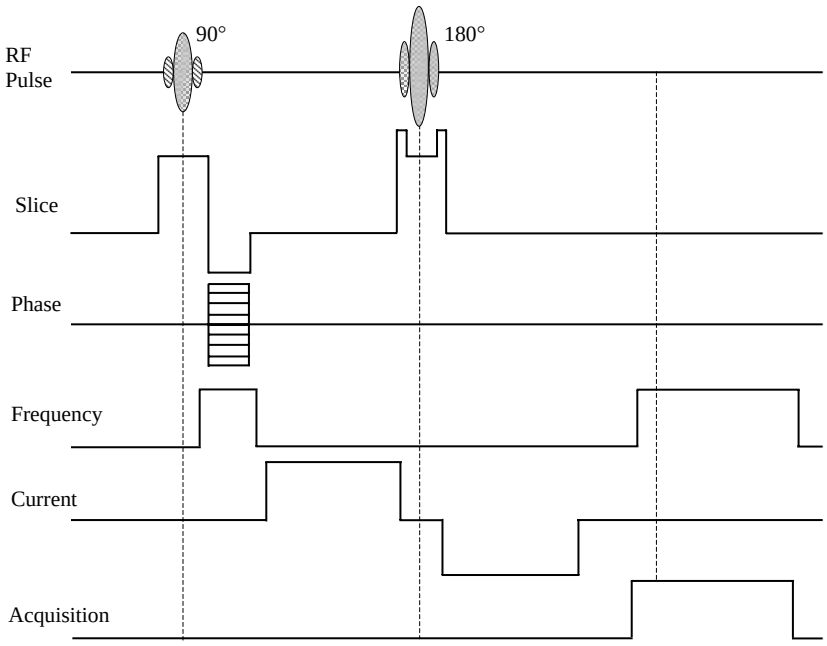

Figure 2. MRCDI pulse sequence used during the experiments.

4.2. Determination of Electric Current Density From Magnetic Flux Density Images

Electric current density can be calculated from magnetic flux density based on Equation (8). In rectangular coordinates the curl operator results in the following relations for J_z, J_x and J_y components of the current density,

$$J_z = \left[\frac{\partial B_y}{\partial x} - \frac{\partial B_x}{\partial y}\right]\frac{1}{\mu_0} \tag{9}$$

$$J_x = \left[\frac{\partial B_z}{\partial y} - \frac{\partial B_y}{\partial z}\right] \frac{1}{\mu_0} \tag{10}$$

and

$$J_y = \left[\frac{\partial B_x}{\partial z} - \frac{\partial B_z}{\partial x}\right] \frac{1}{\mu_0}. \tag{11}$$

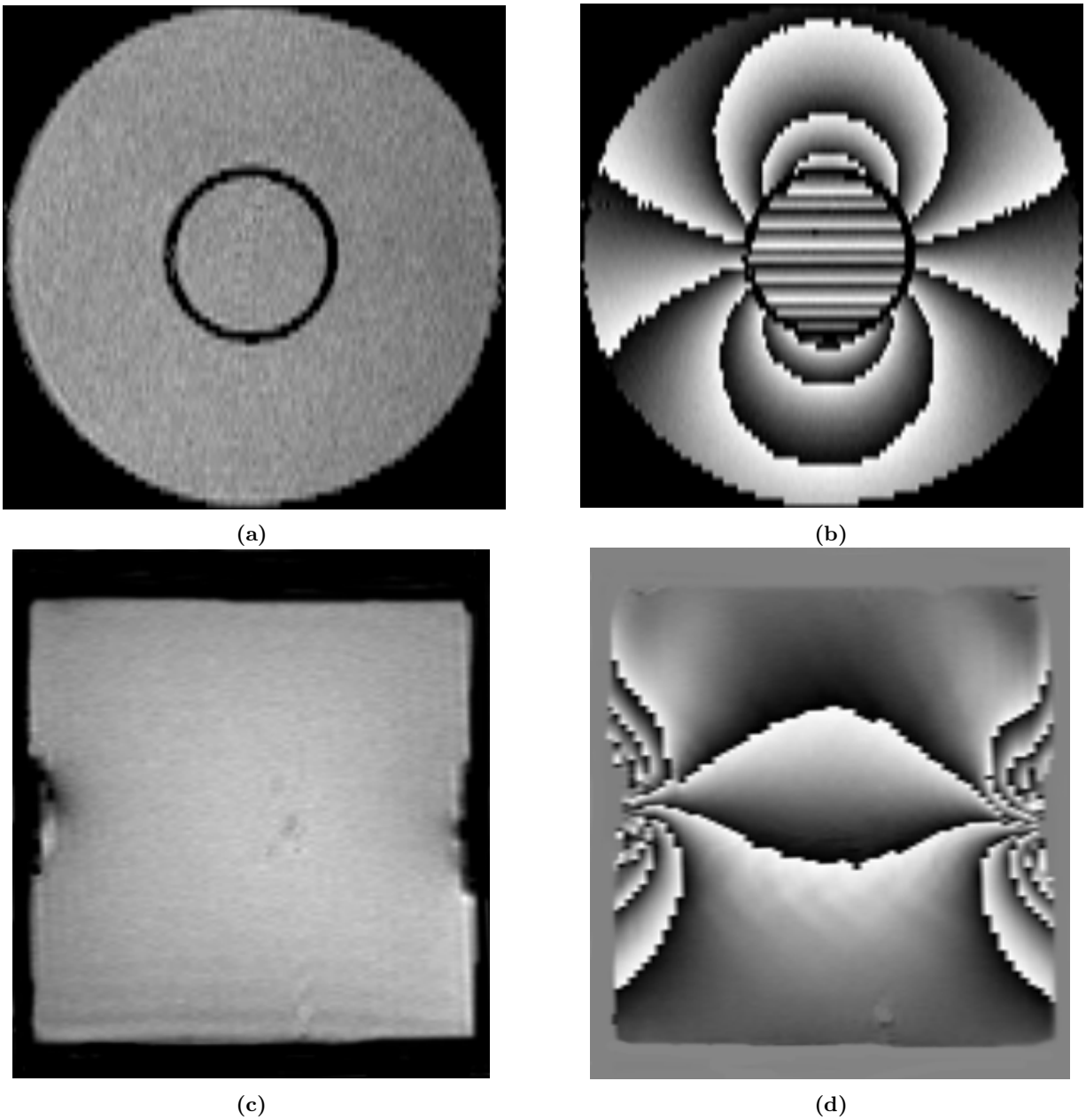

Figure 3. MRCDI (a) magnitude and (b) normalized phase images, acquired from the test phantom given in Figure 1 (a), and (c) magnitude and (d) normalized phase images, acquired from the test phantom given in Figure 1 (b) when a current pulse is applied to the phantom. In the phase images gray scale covers the range from $-\pi$ to π.

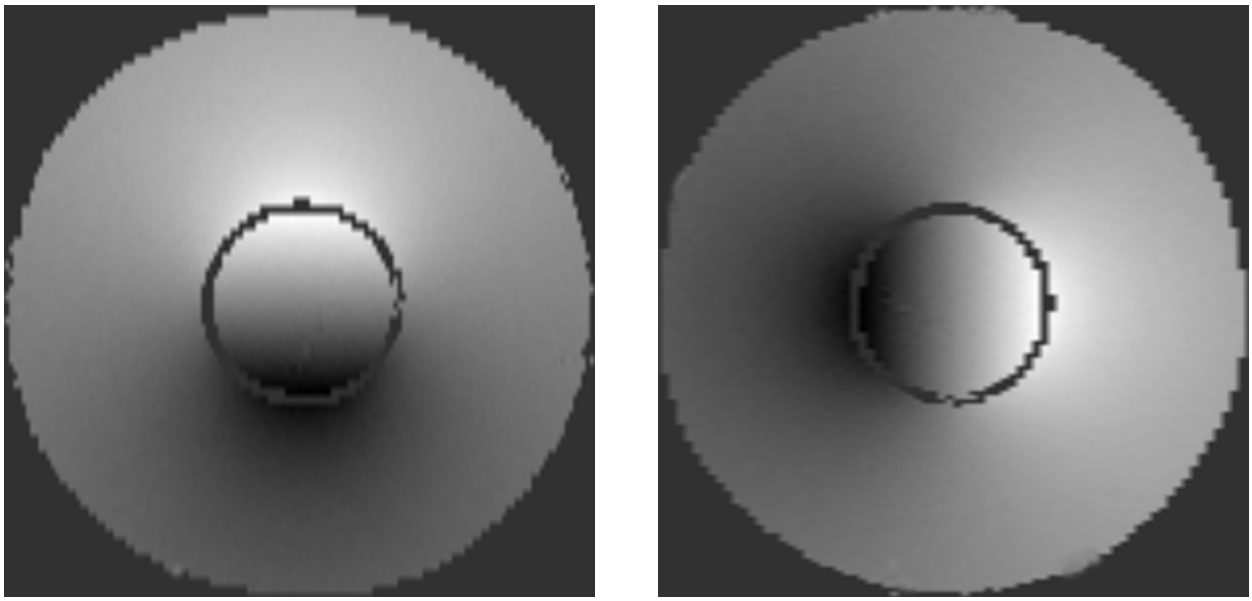

(a) **(b)**

Figure 4. xy-plane MRCDI magnetic flux density images (a) B_x and (b) B_y in the xy-plane for the same image plane as Figure 3 (a).

The directional gradients in Equations (9-11) are calculated by convolving $B_x(x,y)$, $B_y(x,y)$, and $B_z(x,y)$ with (3x3) Sobel operators [15]. Hence, Equation (9) is expressed as,

$$J_z = \left[\frac{\partial B_y}{\partial x} - \frac{\partial B_x}{\partial y}\right]\frac{1}{\mu_0} = \left[\frac{1}{8\Delta x}\begin{vmatrix} -1 & 0 & 1 \\ -2 & 0 & 2 \\ -1 & 0 & 1 \end{vmatrix} * *B_y - \frac{1}{8\Delta y}\begin{vmatrix} 1 & 2 & 1 \\ 0 & 0 & 0 \\ -1 & -2 & -1 \end{vmatrix} * *B_x\right]\frac{1}{\mu_0}. \tag{12}$$

J_x and J_y can be determined similary.

Using a (3x3) template in the computation of the gradient by convolution has the advantage of increased smoothing over (2x2) templates. Using a (3x3) template makes differentiation less sensitive to noise. Weighting the pixel closest to the center by "2" also produces additional smoothing [15]. Scott et al. [7] showed the superiority of the (3x3) template to (2x2) template and reported that the (3x3) template suppressed the ringing due to the truncation of the FID. Larger templates can also be used [16] but (3x3) templates are computationally faster.

5. Results and Discussion

5.1. Imaging of Nonuniform Current Density in a Homogeneous Conductor

Nonuniform current density distribution is imaged, using the homogeneous phantom shown in Figure 1 (a). To measure B_x, a slice orthogonal to the longitudinal axis (xy-plane) of the phantom is imaged when the x-axis of the phantom is aligned parallel with B_0. To measure B_y, this scenario is repeated once more after aligning the y-axis of the phantom parallel with B_0. Figure 5 (a) and (b) show the images of magnetic flux density B_x and B_y, respectively. When imaging B_x, the positive current electrode is located on the left side of the phantom; therefore, B_x is positive in the upper half of the xy-plane and negative in the lower half of the xy-plane, as expected.

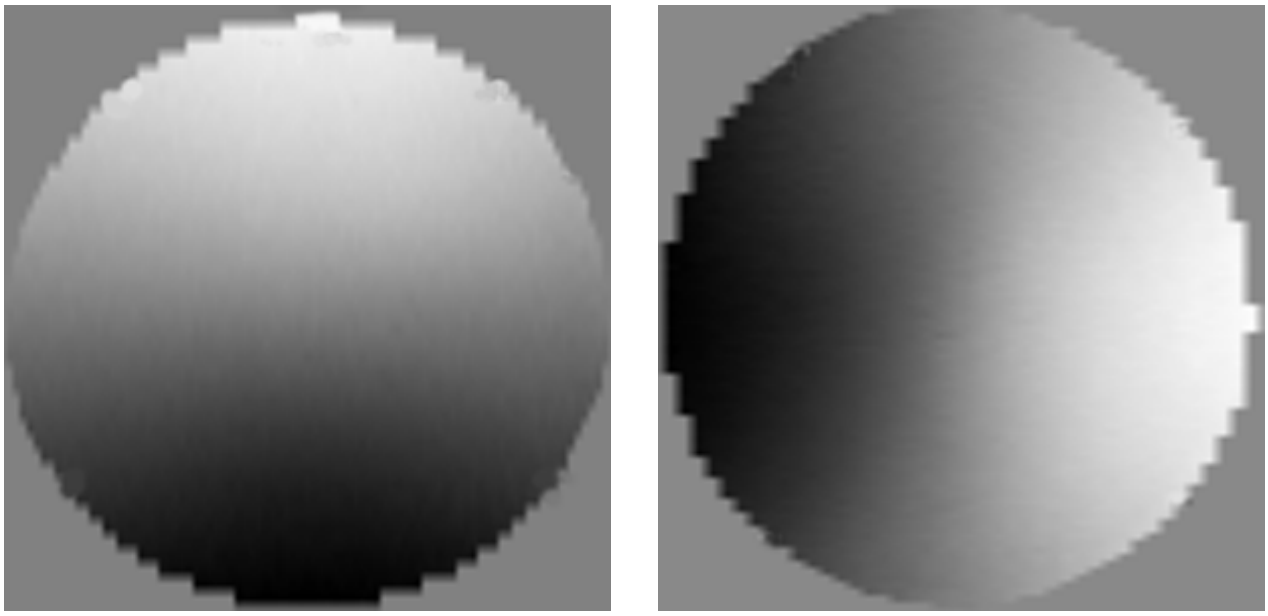

(a) **(b)**

Figure 5. MRCDI magnetic flux density images in (a) x-direction B_x and in (b) y-direction B_y, obtained from the homogeneous phantom. The image are belong to a slice located at the midpoint along the longitudinal axis.

Figure 6 shows the magnitude and the unwrapped phase images at each slice along the z-axis, when the x-axis of the phantom is parallel with B_0. The first slice (Figure 6 (a)) is through the electrode where there is an insufficient MR signal at the center of the image. In the next slice (Figure 6 (b)), which is 7mm from the electrode, current density is almost uniform at the center of the sphere, since the spread of current from the electrode does not occur yet. Therefore, the phase lines are parallel, at the center of the xy-plane, representing a constant $\frac{\partial B_x}{\partial y}$. Figure 6 (c) shows the magnitude and the phase image midway between the electrodes, along the longitudinal axis. The spread of current increases with distance from the electrodes. Images of J_z in several xy-planes along the z-axis can be produced using B_x and B_y images as described in Section 4.2.

5.2. Imaging of Uniform Current Density

Images of uniform current density, at various current levels starting from no current up to 8.8mA, are produced using test phantom 2 (Figure 1(b)). In this phantom, current through the inner tube is forced to be uniform. Therefore, $\frac{\partial B_x}{\partial y}$ is constant and $\frac{\partial B_x}{\partial x}$ is zero inside the inner tube. A transverse plane current density image at the midpoint of the two electrodes, when the amplitude of the current pulse is equal to 0.4mA, is given in Figure 7. In this image, current density measured in the region corresponding to the inner tube is approximately $1.1\mu A/mm^2$. Fluctuations in the region corresponding to the outer tube are due to noise.

The spatial frequency component of the complex image increases with increasing $(I \cdot T_c)$. In this study, T_c is held constant, only the amplitude of the current pulse is changed. Phase images obtained when the x-axis of the phantom is parallel with the main imaging field are given in Figure 8 (a) to (d) for current pulses of 0.4mA, 2.8mA, 6mA and 8mA, respectively. There are no phase wraps, when the applied current is 0.4mA (Figure 8 (a)). The number of phase wraps increases for currents of 2.8mA (Figure 8 (b)) and 6mA

(Figure 8 (c)). Maximum and minimum phase hence, the maximum value of $\mid B_x \mid$ occurs at the interface of the inner and the outer tubes on x=0 line. $\mid B_x \mid$ is zero at the center (x=y=0). Note that for 8mA the phase data inside the inner tube is distorted (Figure 8 (d)). Current density images reconstructed using this phase image and the phase images obtained at current levels higher than 8mA do not represent the correct current density. Causes of this loss of information at high current levels are further investigated in the following section.

5.3. Current Density Effect on k-Space Data

In this section, the effects of increasing current density on k-space data are investigated. To magnify the effect of increasing current density, test phantom 2 is used. As $(I \cdot T_c)$ is increased, the encoded signal into the phase increases the spatial frequency content in Equation (4). Several levels of current, between 0 and 8.8mA are applied to phantom 2. Magnitude of the k-space data, corresponding to the phase images of Figure 8 are shown in Figure 9. In Figure 9, horizontal axis is the frequency encoding direction and the vertical axis is the phase encoding direction. When no current flows through the phantom, k-space data has a signal intensity peak at the center (Figure 9 (a)). Since the object covers more than 1/3 of the field of view (FOV), this is a narrow signal intensity peak. Interesting observations can be made when the applied current is increased. As current is increased (for a constant T_c), an additional phase, equal to $\gamma B_j T_c$, is encoded into the signal originating from the regions of the phantom with a high $\mid B_j \mid$ component (parallel with the main imaging field). This appears as a second signal intensity peak shifted in the phase encoding direction (Figure 9 (b) and (c)). As a result, the signal intensity at the center of the k-space decreases. Magnitude images reconstructed from this data are given in Figure 10. When the current pulse reaches 8mA, the signal intensity originating from the regions with high $\mid B_j \mid$ moves out of the FOV (Figure 9 (d)). Therefore, for current pulses higher than 8mA, the reconstructed magnitude image will have very low or no signal inside the inner tube (Figure 10 (d)). This signal distortion point is determined by the size of the FOV, and $(I \cdot T_c)$. For a given FOV, the current density higher than this level cannot be imaged correctly. Higher currents can be imaged by increasing the FOV, although this will result in a worse resolution.

6. Conclusion

In this study, uniform and nonuniform current density distributions were imaged by using a 2 Tesla MR imaging system, and a standard spin-echo imaging pulse sequence. Current density distribution to be imaged was generated by repetitive application of dc current pulses, synchronized to the imaging sequence. Current densities as low as $1\mu A/mm^2$ were imaged satisfactorily. The lowest current density reported as being measured by Scott et al [7] is $2.4\mu A/mm^2$. Moreover, Scott et al [7] have presented images only away from the current carrying electrodes however, imaging at the electrodes was also achieved in this study. Quantifying current density near the current injecting electrodes is important since high current densities at the electrode tissue interface may result in tissue damage.

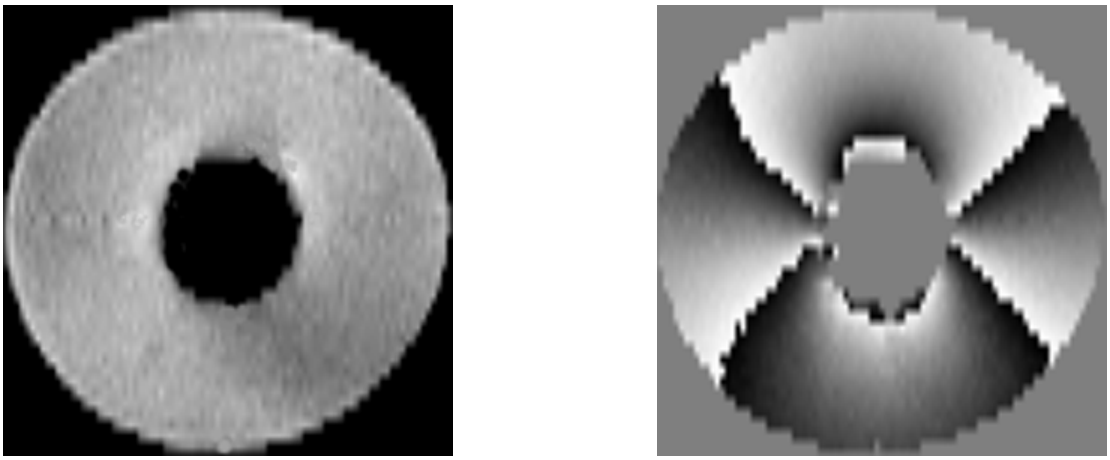

(a)

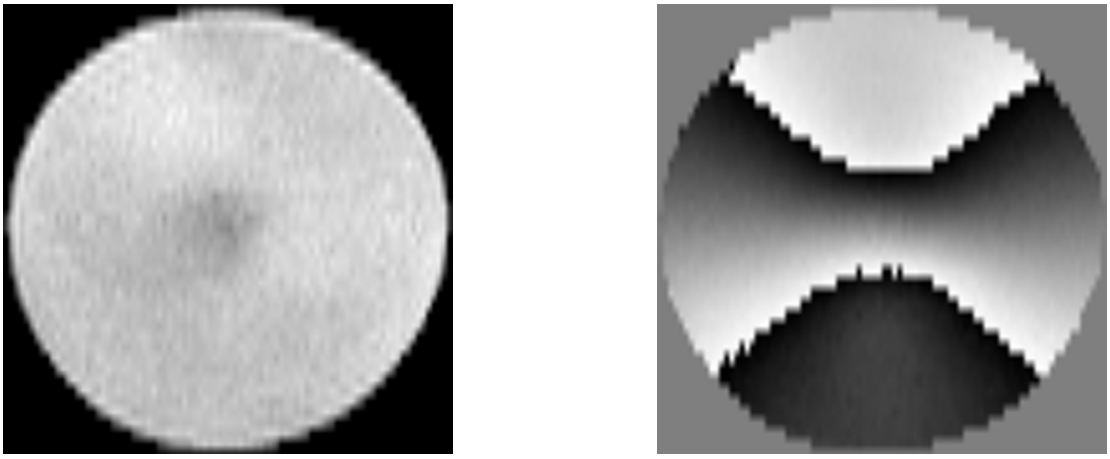

(b)

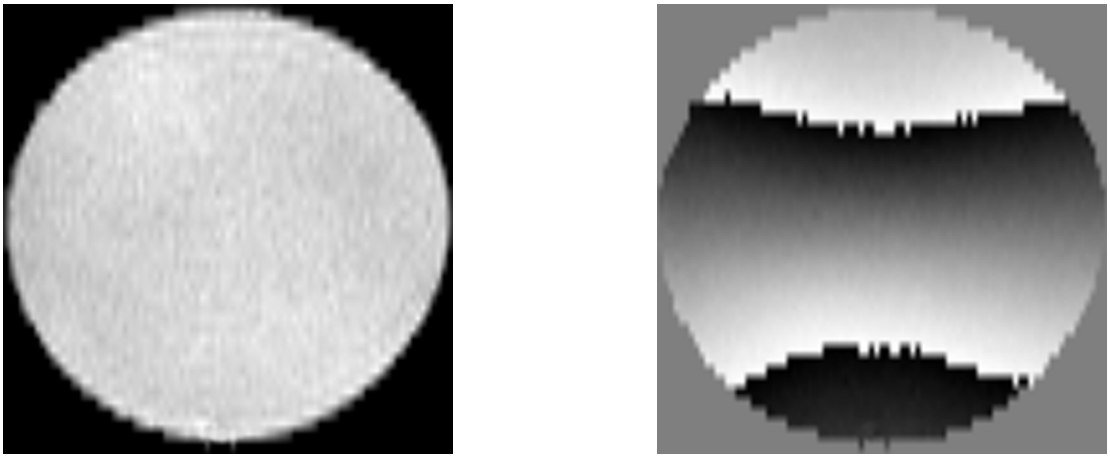

(c)

Figure 6. Magnitude (on the left) and phase images (on the right) in several xy-planes along the longitudinal axis. The first slice is through an electrode (a), the second slice is 7mm. from the electrode (b), the third slice is midway between the electrodes (c).

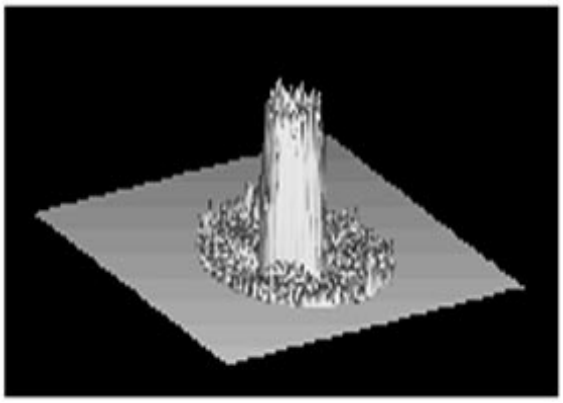

Figure 7. MRCDI current density image acquired from the test phantom of Figure 1 (b) at the midpoint between the two electrodes along the longitudinal axis. Amplitude of the current pulse for this case is equal to 0.4mA.

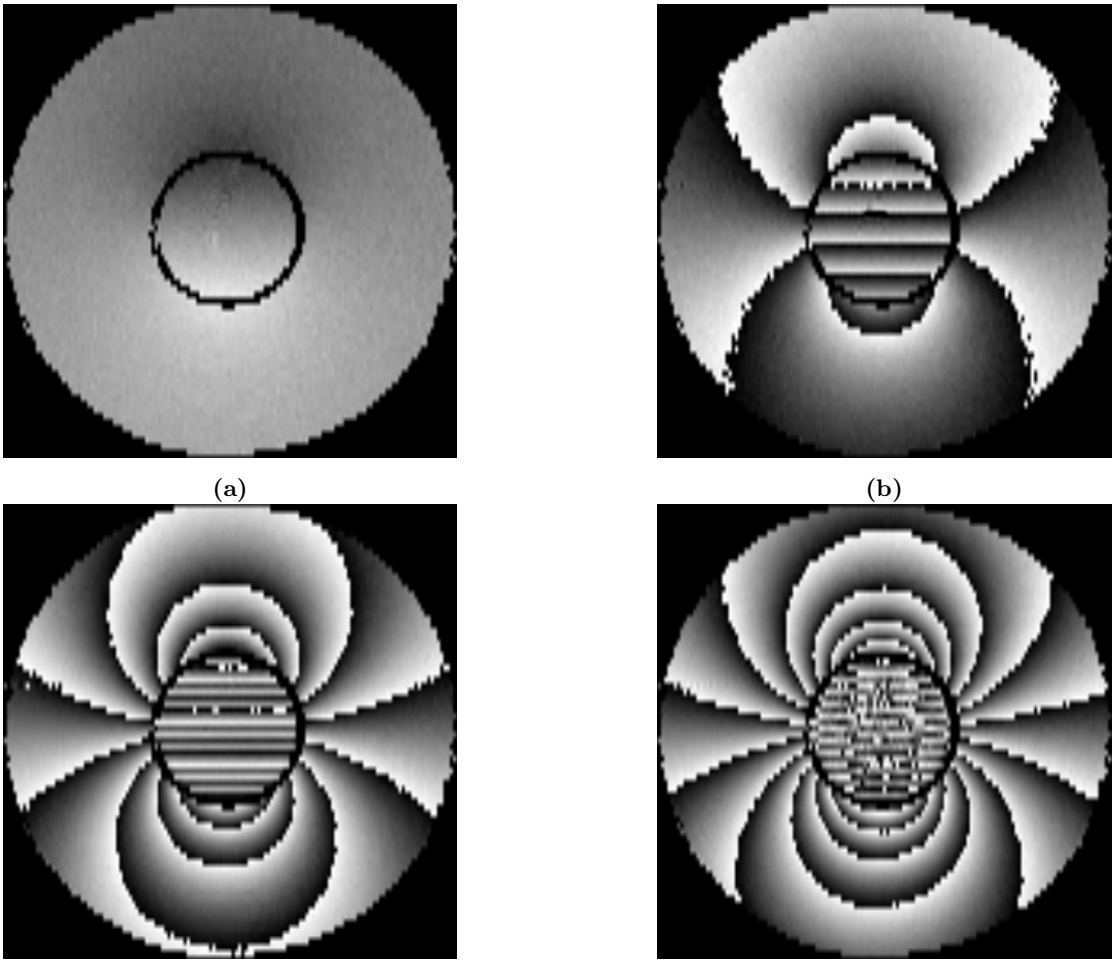

(a) **(b)**

(c) **(d)**

Figure 8. MRCDI phase images acquired from the test phantom of Figure 1 (b), at the midpoint between the two electrodes along the longitudinal axis. Images are taken at current levels of (a) 0.4mA. (b) 2.8mA and (c) 6mA and (d) 8mA. No phase wraps occur for low current levels.

To reconstruct the current density in one direction, components of magnetic flux density in two orthogonal directions (in the plane orthogonal to the direction of current density) are needed. With the method explained in this study, component of the magnetic flux density only parallel with the direction of B_0 can be imaged. Therefore, the sample must be rotated to align two of its axis with the direction of B_0, one axis at a time. This is the major limitation of the technique in applying it to human subjects or large samples, using a conventional MR imaging system. This limitation can be eliminated by utilizing magnets which allow rotation of the imaging field. To overcome the rotation problem, Scott et al [17] implemented a new technique. In this new technique, current density at Larmor frequency and parallel to the direction of B_0 can be imaged without rotating the sample to be imaged. However, imaging current densities at RF frequencies (e.g. approximately 86MHz. at 2 Tesla) may not provide biologically useful information as much as dc current density imaging does.

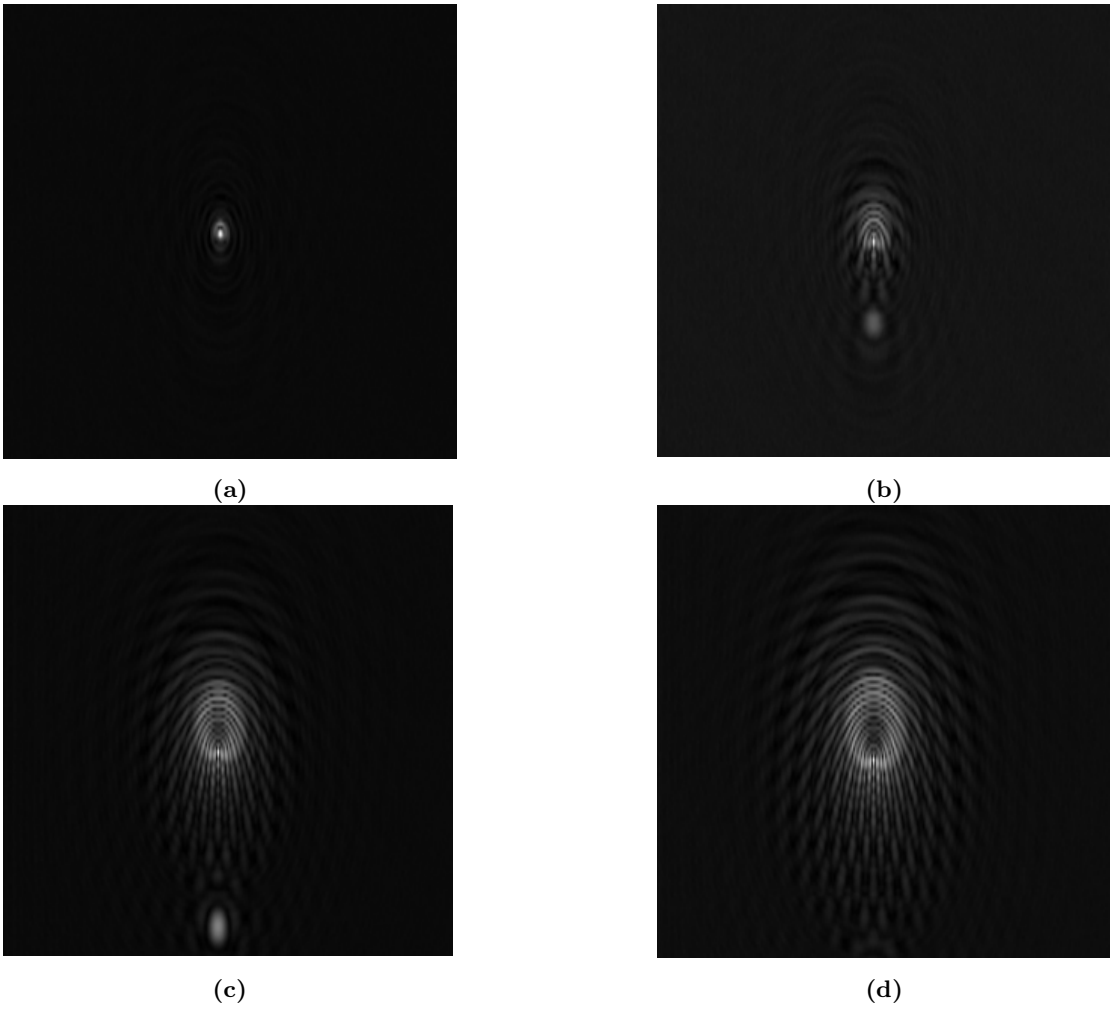

Figure 9. MRCDI k-space images of the same cases as in Figure 8.

MRCDI has potential biomedical applications in better understanding of externally applied electric fields to human body. For example, defibrillation efficacy may be improved by finding optimum electrode configurations which create a larger voltage gradient field across the heart with a better homogeneity. Therefore, MRCDI may be useful in determining optimum electrode size, shape and position for cardiac defibrillation. Imaging current density underneath the current injecting electrodes also becomes important

in this prospective application.

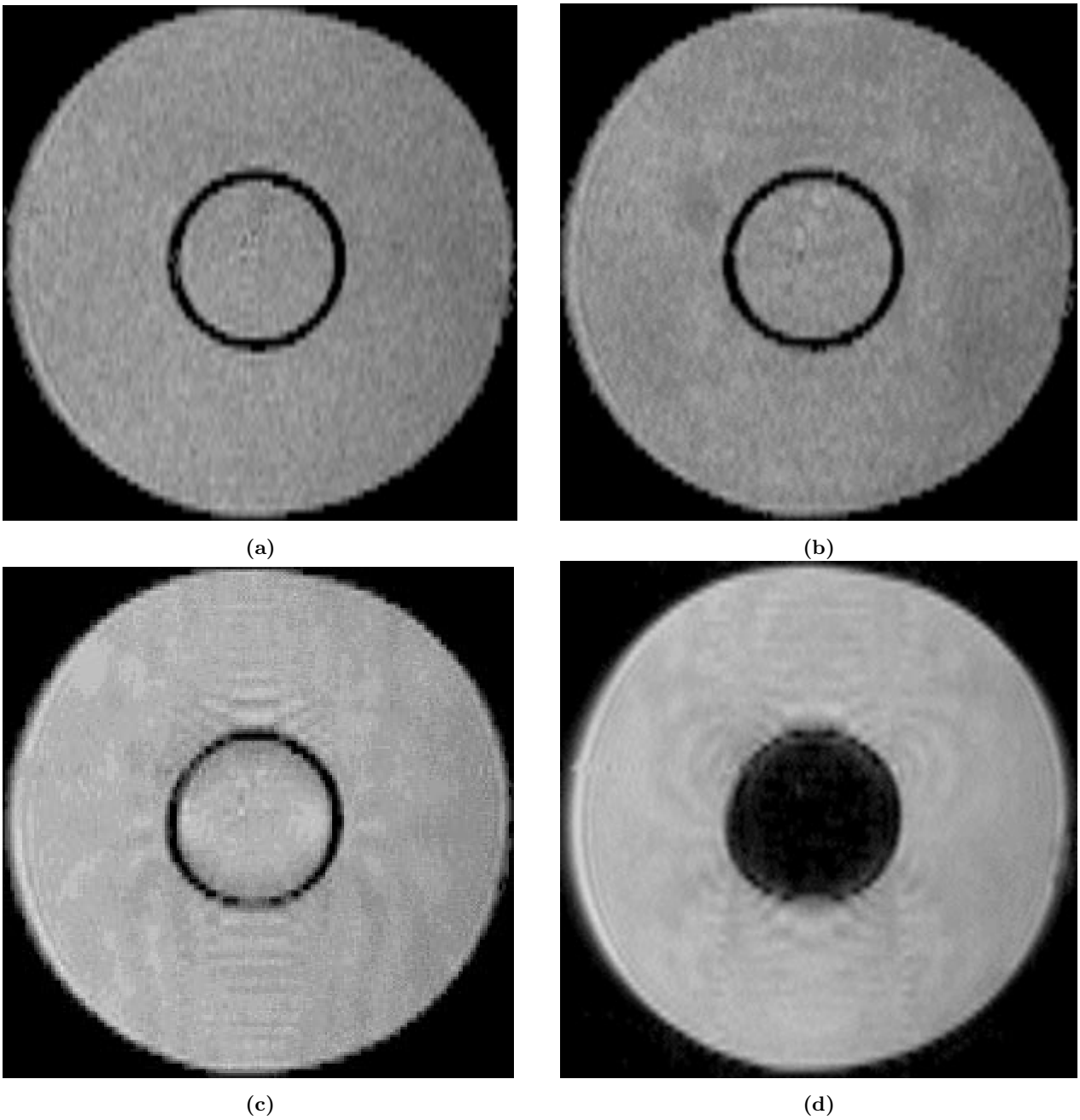

(a) **(b)**

(c) **(d)**

Figure 10. MRCDI magnitude images of the same cases as in Figure 8.

By measuring current density inside a volume conductor, which is generated by currents applied via a surface electrode pair (lead), lead-sensitivity map of that electrode pair can be obtained. Measurement of lead-sensitivity maps can be useful in bio-electric imaging, and bio-impedance measurements.

Spatial distribution of electrical conductivity and current density are directly related. Biological tissues have different electrical properties and the electrical properties of some tissues, especially cardiac and lung tissues change with their functional state. It may be possible to obtain anatomical and functional information from current density images [5]. Accurate determination of current density may also lead to

accurate high resolution conductivity images.

Acknowledgment

This work was supported in part by National Institutes of Health research grant RR-02305.

References

[1] Ideker R E, Wolf P D, Alferness C, Karassowska W and Smith W M 1991 "Current concepts for selecting the location, size and shape of defibrillation electrodes" *PACE* **14** 227-40.

[2] Kneppo P and Titomir L I 1992 "Topographic concepts in computerized electrocardiology" *Critical Reviews in Biomedical Engineering* **19(5)** 343-418.

[3] Province R A, Fishler M G and Thakor N V 1993, "Effects of defibrillation shock energy and timing on 3-D computer model of heart" *Annals of Biomedical Engineering* **21** 19-31.

[4] Geselowitz D B, 1971, "An application of electrocardiographic lead theory to impedance plethysmography" *IEEE Transaction on Biomedical Engineering* **18** 38-41.

[5] Webster J G (Ed) 1990 *Electrical Impedance Tomography* (Adam Hilger) p.224.

[6] Joy M, Scott G C and Henkelman R M 1989 "In vivo detection of applied electric currents by magnetic resonance imaging" *Magnetic Resonance Imaging* **7** 89-94.

[7] Scott G C, Joy M L G, Armstrong R L and Henkelman R M 1991, "Measurement of nonuniform current density by magnetic resonance" *IEEE Transactions on Medical Imaging* **10(3)** 362-74.

[8] Scott G C, Joy M L G, Armstrong R L and Henkelman R M 1992, "Sensitivity of magnetic resonance current-density imaging" *J. Magnetic Resonance* **97** 235-54.

[9] Mansfield P and Morris P G 1982 *NMR Imaging in Biomedicine* (Academic Press) pp.32-80.

[10] Holz M and Muller C 1980 "NMR measurements of internal magnetic field gradients caused by the presence of an electric current in an electrolyte solution" *J. Magnetic Resonance* **40** 595-99.

[11] Maudsley A A, Simon H E and Hilal S K 1984 "Magnetic field measurement by NMR imaging" *J. Physics E.* **17(3)** 216-220.

[12] Bolinger L, Prammer M G and Leigh JS, Jr. 1988 "A multiple-frequency coil with a highly uniform B_1 field" *J. Magnetic Resonance* **81** 162-6.

[13] Alderman D and Grant D M 1979 "An efficient decoupler coil design which reduces heating in conductive samples in superconducting spectrometers" *J. Magnetic Resonance* **36** 447-51.

[14] Liang Z P 1996 "A model-based method for phase unwrapping" *IEEE Transactions on Medical Imaging* **15(6)** 893-7.

[15] Gonzalez R C and Woods R E 1992 *Digital Image Processing* (Addison-Wesley Publishing Company), pp. 418-21.

[16] Kirsch 1971 "Determination of the constituent structure of biological images" *Comput. Biomed. Res.* **4** 315-328.

[17] Scott G C, Joy M L G, Armstrong R L and Henkelman R M 1995, "Rotating frame RF current-density imaging" *Magnetic Resonance in Medicine* **33** 355-69.